Available online at www.sciencedirect.com
ScienceDirect
Trans. Nonferrous Met. Soc. China 35(2025) 4065−4083
Transactions of Nonferrous Metals Society of China
www.tnmsc.cn

Microstructure and corrosion behavior of laser surface melting treated Mg−Zn−Y alloy

Zhen-zhen PENG[1], Min-heng XU[1], Xiao-hong SHAO[2],
Xiao YANG[1], Heng-hu ZHAO[1], Zhi-min LIANG[1], Dian-long WANG[1], Ying LIU[1]

1. Hebei Key Laboratory of Material Near-Net Forming Technology, School of Materials Science and Engineering,
Hebei University of Science and Technology, Shijiazhuang 050018, China;
2. Shenyang National Laboratory for Materials Science, Institute of Metal Research,
Chinese Academy of Sciences, Shenyang 110016, China

Received 30 March 2024; accepted 13 December 2024

Abstract: A laser surface melting (LSM) technology was applied to enhancing the corrosion resistance of a Mg−Zn−Y alloy containing large and discontinuous long-period stacking-ordered (LPSO) phases. The microstructural evolution and solidification behavior of this alloy during LSM were studied. It was demonstrated that the significantly reduced corrosion rate of the alloy after LSM, can be attributed to the disappearance of the original micron-sized LPSO phase and a decrease in the grain size from 300 to 15 μm. The refined grains were composed of three adjacent zones, namely the β eutectic phase zone, the W phase zone, and the lamellar structures zone, which formed sequentially during the rapid cooling process. The dendritic lamellae grew along the basal plane of the magnesium matrix and were separated by supersaturated α-Mg phases. Ultimately, the disappearance of large primary batteries and grain refinement improved the corrosion resistance of the Mg−Zn−Y alloy.

Key words: Mg−Zn−Y alloy; microstructural evolution; solidification behavior; laser surface melting; corrosion resistance

---

1 Introduction

Magnesium (Mg) and its alloys have garnered significant attention because of the increasing demand for lightweight structural materials in the global aerospace and land transportation industries [1−3]. However, Mg alloys tend to exhibit a poor corrosion resistance, a low ductility, and a low strength compared to other structural metals, which limits their application [4,5]. The mechanical properties of Mg alloys are typically improved by utilizing the fine-grain reinforcement or the reinforcing effect of the secondary phase [6−11]. However, these methods have not significant effect on the corrosion resistance of Mg alloys [12−14].

The corrosion resistance characteristics of Mg alloys are often associated with the activity of the Mg, the distribution of the surface microstructure, and the protective capacity of the surface layer [15]. Mg alloys can be rendered more corrosion resistant by altering the distribution state of the micro-galvanic cells that form on the alloy surface during corrosion [16,17], by enriching the surface of the alloy with beneficial solute elements such as Al and Zn [18,19], or by inducing the formation of coatings on the surface [20−22]. For example, upon

---

Corresponding author: Xiao-hong SHAO, Tel: +86-13709814280, E-mail: xhshao@imr.ac.cn;
Zhi-min LIANG, Tel: +86-18931102859, E-mail: lianghebust@163.com

https://doi.org/10.1016/S1003-6326(25)66930-5

1003-6326/© 2025 The Nonferrous Metals Society of China. Published by Elsevier Ltd & Science Press
This is an open access article under the CC BY-NC-ND license (http://creativecommons.org/licenses/by-nc-nd/4.0/)

the addition of rare earth elements, the distribution of the metallographic organization of the Mg alloy can be altered. This resulted in finer and more uniformly distributed primary cell characteristics, thereby reducing the redox effect of the galvanic coupling [23]. In addition, the gradient-layered structure formed by high-temperature treatment on the surface of the WE43 Mg alloy was found to play a significant role in improving its corrosion resistance [24]. It has also been reported that plasma electrolytic oxidation produced an Al-rich, low-porosity, corrosion-resistant dense layer with an average thickness of 50 μm on the surface of the AZ91 Mg alloy in an alkaline phosphate–aluminate electrolyte [25]. However, these conventional methods are complex and time-consuming.

As a possible alternative to conventional methods, laser surface melting (LSM) has attracted extensive attention because of its various advantages, including fast and flexible processing, facile automation, excellent reproducibility, and no requirement for surface pretreatment [26,27]. In addition, LSM is an efficient approach for altering the surface microstructures and enhancing the corrosion resistance properties of metallic materials via two key mechanisms. In the first mechanism, a passivation film was formed on the alloy surface by LSM, such as in the case of the AZ31 alloy, whose surface was enriched with Al after LSM. Since Al element was more likely to form a passivation film, the corrosion rate of the alloy was reduced [28]. In the second mechanism, a melted layer was formed on the surface of the alloy using LSM. After LSM, the average grain size of the AZ91D alloy was found to decrease from 200 to 2 μm, and the original discontinuously distributed large β-$Mg_{17}Al_{12}$ phase became extremely small and distributed continuously in a network structure along grain boundaries. The grain refinement and the presence of small β-$Mg_{17}Al_{12}$ phases led to a homogeneous distribution of the surface potential, and separated Mg from the corrosive medium to enhance the corrosion resistance of the alloy [29]. It has also been reported that the corrosion resistances of AM60B and WE43 alloys were enhanced after LSM, following a mechanism similar to that of the AZ91D alloy, which involved enriching alloy elements in the α-Mg matrix, refining grains, and redistributing secondary phases within the modified layer [30,31].

Owing to their favorable mechanical properties at both room temperature and high temperatures, Mg alloys containing the long-period stacking ordered (LPSO) phase have been a focal point of research over the past few decades. It has been reported that the LPSO blocks presented in the as-cast alloy transform into lamellar or rod-shaped morphologies after various heat treatments [32]. These structures exhibit various deformation mechanisms and significantly improve the mechanical properties of the Mg alloys [33,34]. However, the corrosion resistance properties of Mg alloys are negatively affected by the LPSO phase [35]. Since the electrode potential of the LPSO phase is higher than that of the α-Mg phase [36], it will act as a cathode to accelerate the corrosion process of the Mg alloys, with the corrosion rate increasing with an increasing volume fraction of the LPSO phase [37]. Although the corrosion resistances of Mg alloys have been enhanced by altering the morphology of the LPSO phase [38,39], Mg alloys containing discontinuous or large LPSO phases still encounter significant corrosion issues.

The purpose of this work was therefore to refine the LPSO phase on the surface of the Mg−Zn−Y alloy by LSM, reduce the size of large primary batteries composed of large LPSO phases and Mg grains, and refine the grains to enhance the corrosion resistance. Electrochemical and immersion tests were conducted to analyze the surface electrochemical characteristics and corrosion properties of the Mg−Zn−Y alloy after LSM. By investigating the microstructural transition during LSM, including the changes in the grain size, grain shape, and phase transformation, the influences of fast cooling on the microstructure and phase were analyzed. Furthermore, the mechanism responsible for the enhanced corrosion resistance was investigated.

2 Experimental

2.1 Material preparation

The $Mg_{97}Zn_1Y_2$ (at.%) alloy was prepared by melting high purity Mg, Zn, and a Mg−30wt.%Y master alloy in an ordinary resistance furnace. The dimensions of the as-cast ingot were about d50 mm × 200 mm. Subsequently, 10 mm × 10 mm × 10 mm cuboids were cut from the cast alloy and successively ground using $1000^{\#}$ and $2000^{\#}$ SiC sandpapers, polished with 1 μm-grit diamond polishing paste, and then subjected to laser treatment, as outlined schematically in Fig. 1.

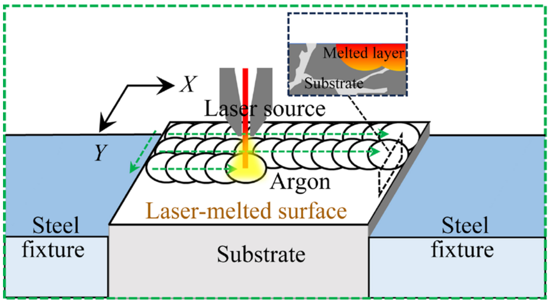

Fig. 1 Schematic diagram of LSM experiment

More specifically, for the LSM experiment, a YLR−1000−SM fiber laser (IPG, Germany) was employed with argon serving as the shielding gas. The sample surface was scanned by the laser with a focus diameter of 28 μm and a 1 mm defocus. To ensure the homogeneity of the surface microstructure, the overlap rates of the laser in both the transverse (R_X) and longitudinal (R_Y) directions were set to 10%. R_X and R_Y were calculated using Eqs. (1) and (2), which are based on the laser focus diameter (d), the laser frequency (f), the laser movement speed in the transverse X-direction (v_X), and the row spacing in the longitudinal Y-direction (L_Y), as follows:

$$R_X=\left(\left(d-\frac{v_X}{f}\right)\Big/d\right)\times 100\%\approx 10\% \tag{1}$$

$$R_Y=\frac{d-L_Y}{d}\times 100\%\approx 10\% \tag{2}$$

The samples were categorized into four groups, namely the as-cast sample (as-cast), the 150 W laser-treated sample (S150), the 160 W laser-treated sample (S160), and the 170 W laser-treated sample (S170). The laser processing parameters employed in the current LSM experiments are listed in Table 1.

2.2 Electrochemical testing

Electrochemical testing was conducted using a Princeton multichannel electrochemical workstation (PARSTAT MC, USA) equipped with a Versa-Studio software in a 3.5 wt.% NaCl solution at 20−30 °C. A classical three-electrode system was employed, with a platinum electrode as the auxiliary electrode and a saturated calomel electrode as the reference electrode. The samples were embedded in acrylic adhesives, and the laser-treated surface of 1 cm^2 was used as the working electrode.

Electrochemical impedance spectroscopy (EIS) measurements were performed potentiostatically in a 3.5 wt.% NaCl solution at the open circuit potential (OCP). The frequency range was set from 100 kHz to 0.1 Hz, and a sinusoidal waveform with an amplitude of 10 mV was applied, collecting 10 points per decade at a scan rate of 5 mV/s. The EIS spectra were fitted using the ZView2 software. The potentiodynamic polarization tests were performed over a potential range of ±300 mV relative to the OCP at a scan rate of 1 mV/s.

2.3 Immersion testing

The as-cast and laser-treated samples were encapsulated with acrylic adhesives for cold setting, exposing only the test area (1 cm^2), and then immersed in a 3.5 wt.% NaCl solution (400 mL) for 4, 8, 12, 16, 20, and 24 h, respectively. After immersion for a specific duration, the corrosion products were removed from the sample using a boiling solution of 200 g/L CrO_3 + 10 g/L $AgNO_3$. The samples were then washed by anhydrous alcohol and dried in a drying oven at 90 °C for 10 min. The corrosion rates of the samples were determined by comparing the masses of the samples before and after immersion.

2.4 Microstructural characterization

The morphologies and elemental distributions of the surfaces and cross-sections of the samples before and after LSM were analyzed using optical microscopy (OM) and scanning electron microscopy (SEM, S4800) equipped with an energy-dispersive X-ray (EDX) analyzer. The cross-sectional samples were prepared by embedding the samples in acrylic adhesives, leaving a side parallel

Table 1 Parameters used in LSM experiments

Power, P/W	Frequency, f/Hz	Duty ratio, D/%	Scanning speed, v_X/(mm·s^{-1})	Vertical spacing, L_Y/mm	Argon flow rate, Q/(L·min^{-1})
150~170	1000	20	25	0.025	7

to the X direction uncoated. The sides were then ground with SiC sandpaper, polished using 1 μm-grit diamond polishing paste, and corroded using specific corrosive solution prior to performing the OM observation. The phases in the melted layer after LSM were examined by X-ray diffractometry (XRD).

Electron back-scattered diffraction (EBSD) test was used to measure the grain size of the laser-treated region. Ion-beam polishing was performed after sanding the side of the laser-treated sample with sandpaper. The polishing area was approximately 200 μm × 50 μm, including the entire melted layer and part of the matrix area. After ion-beam polishing, the polished area was observed using EBSD.

The microstructure and phase distribution of the melted layer were further investigated using spherical aberration-corrected transmission electron microscopy (AC-TEM, JEOL ARM 200) and field-emission transmission electron microscopy (FE-TEM, FEI Talos F200X) with four energy-spectrum detectors. The TEM sample was prepared by cutting a 0.8 mm-thick piece from the surface of the laser-treated alloy. This sample was then ground from the opposite side of the melted layer using $2000^{\#}$ SiC sandpaper to give a thickness of <30 μm. The pre-thinned samples were subsequently punched to produce thin slices of d3 mm, and these slices were further thinned and perforated by the application of ion beams from the opposite side of the laser-treated surface. To avoid the influence of temperature during ionic thinning, the above experiments were conducted using a precise ion polishing system (PIPS 695) equipped with a liquid-nitrogen cooling stage.

3 Results

3.1 Microstructure and surface composition

3.1.1 Surface and cross-section microstructure characteristics before and after LSM

The OM and SEM images of various samples are shown in Fig. 2. It can be seen from Figs. 2(a) and (b) that discontinuous LPSO phases were distributed at the boundaries of the α-Mg matrix in the as-cast alloy. After LSM, the LPSO phases could not be distinguished in the images, and as the laser power was increased, the surfaces became clean, and the shape of the laser spot became clearer, as indicated in Figs. 2(c−h).

The surface elemental distributions analyzed by EDS mapping of the as-cast alloy and the laser-treated (S160) sample are shown in Figs. 3(a) and (b), respectively. The S160 sample was selected because the subsequent corrosion tests showed that it exhibited an excellent corrosion resistance. Mg, Zn, and Y were found to be more uniformly distributed in the S160 sample than in the untreated alloy, indicating that the LPSO phase may have disappeared during LSM. More specifically, Zn was almost uniformly distributed in the S160 sample, while Y was no longer concentrated within the distribution range of the original LPSO phase.

The cross-sectional morphology of each group of samples was analyzed using OM, as shown in Fig. 4. In the as-cast alloy, the discontinuous LPSO phase is clearly distributed throughout the alloy, while the acrylic adhesive is present beneath the alloy (Fig. 4(a)). In the laser-treated alloys, melted layers can be observed in all samples, as shown in Figs. 4(b−g). Since the laser energy is distributed in

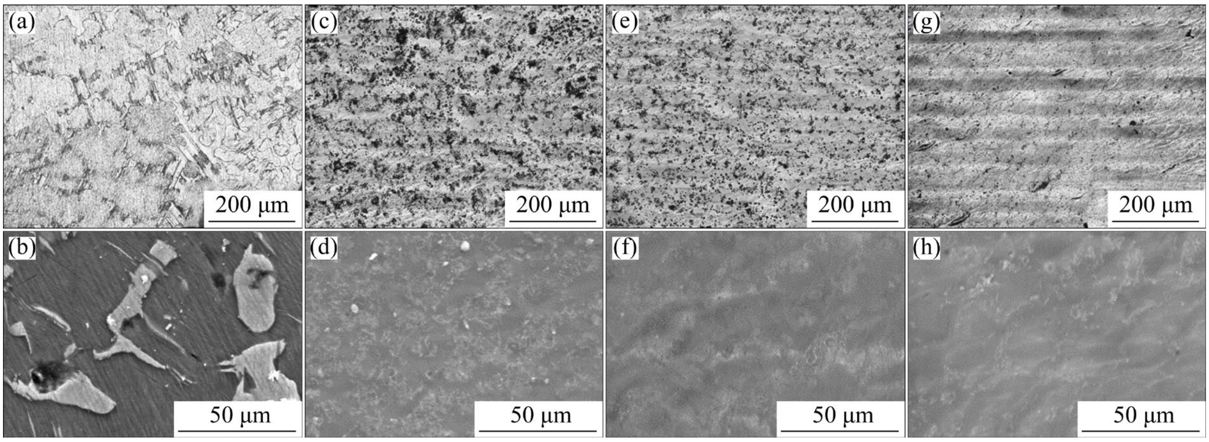

Fig. 2 OM (a, c, e, g) and SEM (b, d, f, h) images of various samples: (a, b) As-cast; (c, d) S150; (e, f) S160; (g, h) S170

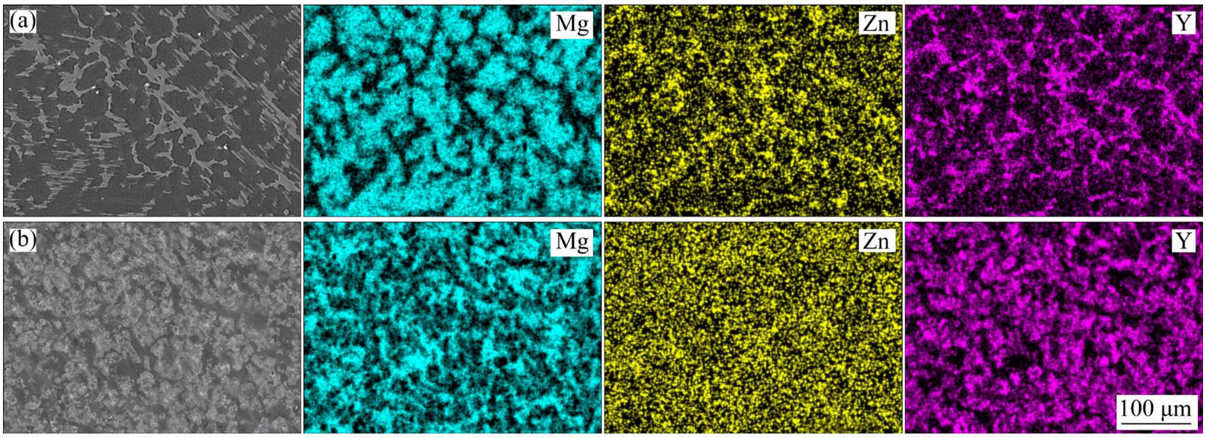

Fig. 3 SEM images and corresponding EDS mappings of different samples: (a) As-cast; (b) S160

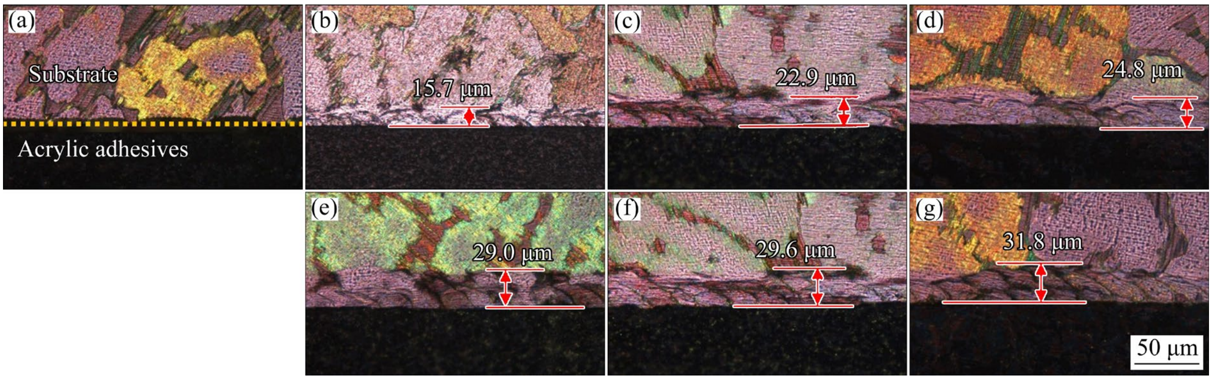

Fig. 4 OM images of cross-sections of as-cast and laser-treated samples: (a) As-cast; (b, e) S150; (c, f) S160; (d, g) S170; (b−d) Melted layer of α-Mg phases; (e−g) Melted layer of LPSO phases

a Gaussian manner, the heat generated at the center of the laser spot is higher than that in the surrounding area [40], which leads to a bowl-shaped cross-sectional morphology of the melted zone. In the S150 sample, the α-Mg melted layer is thin, and the laser spot traces in the melted layer are not obvious, as can be seen from Fig. 4(b). Upon increasing the laser power, the melted layer and the laser spot trace in the melted layer become more evident, as shown in Figs. 4(c−g). In addition, the thicknesses of the melted layers in LPSO phases of various samples are clearly greater than those in the α-Mg phases (see Figs. 4(b, e), Figs. 4(c, f), and Figs. 4(d, g). Considering a previous report that the LPSO phase enhances the thermal conductivity of the Mg alloy [41], the above observations could be attributed to the fact that the LPSO phases absorb a greater amount of laser heat than the α-Mg phases during LSM.

3.1.2 Phase compositions

The XRD experiments were conducted to distinguish the phases present on the sample surfaces before and after LSM at different laser powers, and the results are presented in Fig. 5. Prior to LSM, the sample was composed of Mg matrix and LPSO phase (2θ=34.0°−35.0° and 56.5°−58.0°, respectively), while after LSM treatment, no obvious peaks corresponding to the LPSO phase were observed, as shown in Fig. 5(a). Detailed observation of the XRD results confirmed that the LPSO phase disappeared after laser treatment under different laser powers, as shown in Figs. 5(b) and (c).

3.2 Corrosion resistance enhancement by LSM

3.2.1 Electrochemical behavior

Figure 6 shows the Nyquist plots, phase-angle Bode plots, and polarization curves of the as-cast and laser-treated samples to verify their surface corrosion properties. As shown in the Nyquist plots in Fig. 6(a), the capacitance loop in the high-frequency region of the EIS is associated with the charge-transfer process on the surface of the working electrode, which is influenced by the

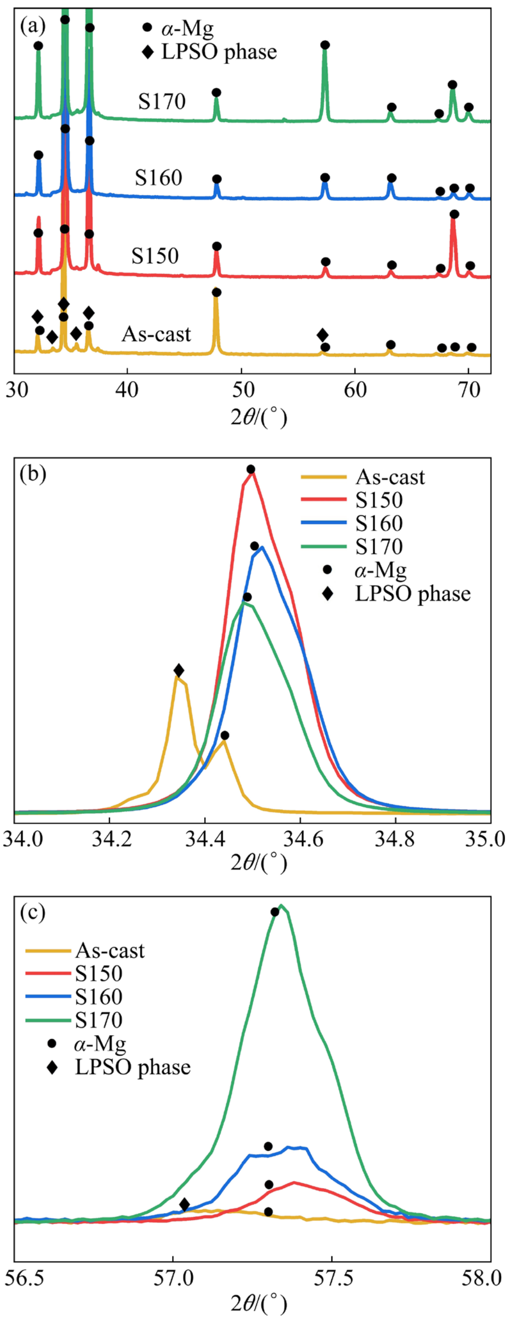

Fig. 5 XRD patterns of different samples before and after LSM treatment: (a) 2θ=30.0°−60.0°; (b) 2θ=34.0°−35.0°; (c) 2θ=56.5°−58.0°

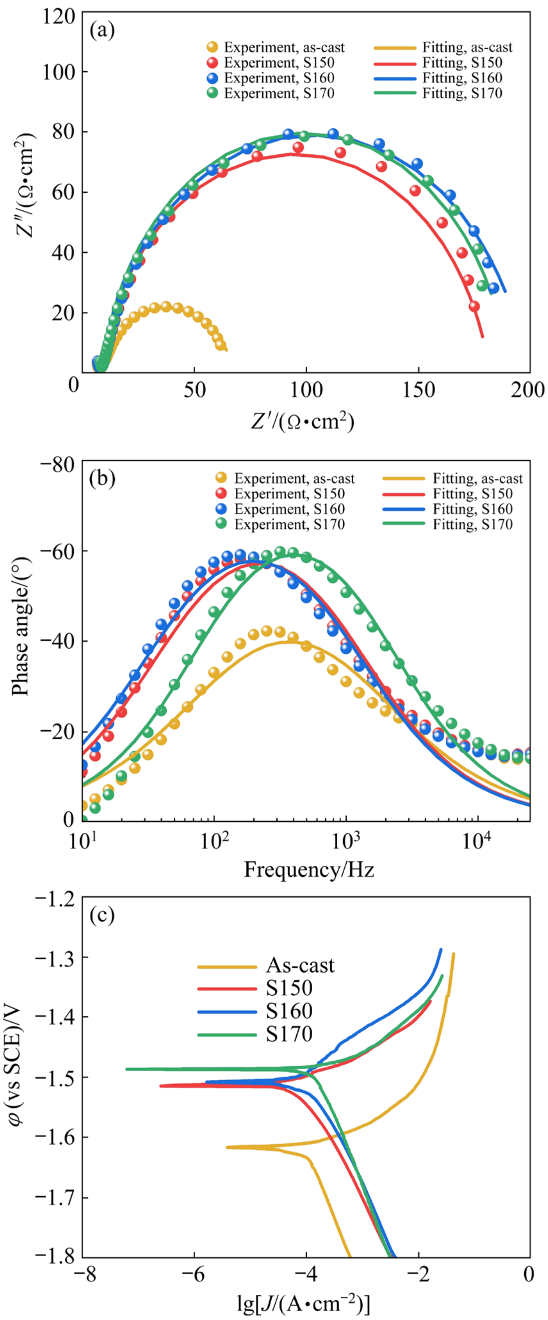

Fig. 6 Electrochemical properties of different samples: (a) Nyquist plots; (b) Phase angle Bode plots; (c) Polarization curves

electrical-double layer between the NaCl electrolyte and the melted layer. The diameters of the high-frequency capacitance loops of the laser-treated samples are all greater than those of the as-cast Mg−Zn−Y alloy, as shown in Fig. 6(a), indicating that the LSM treatment slows down the metal dissolution rate. The phase-angle Bode diagram confirms the capacitive nature of the electrical-double layer formed on the surface, as shown in Fig. 6(b). The voltage across an ideal capacitor lags the current flowing through it by 90°; thus, the phase angle of an ideal capacitor is generally −90° in the phase-angle Bode plot. Therefore, the larger the phase angle is, the larger the capacitance is. More negative phase angles in the middle-frequency range (10^1−10^3 Hz) imply a more capacitive nature of the melted layer. Consequently, an increase in the capacitance of the interface region of the sample surface results in greater hindering effects on the test current, whilst simultaneously providing stronger protection effects on the base metal. As shown in Fig. 6(b), the samples treated at various laser powers exhibit larger phase angles (about −60°) than that of the as-cast sample (about −40°), although no significant differences exist between the phase angles of the samples prepared at different laser powers.

The polarization curves of various sample groups in a 3.5 wt.% NaCl solution are shown in Fig. 6(c), wherein it can be seen that the laser-treated samples exhibit lower current densities than the as-cast alloy, which is consistent with the EIS results. These results unambiguously demonstrate that the laser-treated alloy exhibits superior corrosion resistance properties than the untreated alloy.

The EIS data were further analyzed using equivalent circuit modelling. Figure 7 depicts the equivalent electrical circuit in a 3.5 wt.% NaCl solution for each sample. In this circuit, R_1 represents the resistance of the corrosion solution, and R_2 represents the charge transfer resistance between the corroding solution and the working electrode. A constant-phase element (CPE_1), which can be considered as the capacitance of the electrical-double layer, was used instead of a capacitor to accurately simulate the capacitive response of the system [42]. A parallel combination of R_2 and CPE_1 was followed by a series connection with R_1. After fitting using ZView2 software, the fitting error of each circuit element was determined (<10% in most cases), and the obtained fitting results are presented in Table 2. It can be seen that the R_2 values of the laser-treated samples were significantly increased compared to that of the as-cast alloy; more specifically, the R_2 values of the 160 W laser-treated samples and the as-cast alloy were 190.00 and 60.78 $\Omega\cdot cm^2$, respectively. Considering that a larger R_2 value between the solution and the working electrode represents slower dissolution of the working electrode, the obtained results indicate that the laser-treated melted layer exhibited a good protective effect against corrosion. In addition, the corrosion resistances of the samples treated at different laser powers were relatively comparable. However, since the S160 specimen exhibited the largest R_2 value among all the laser-treated samples, it was selected for the subsequent study of the corrosion behavior during immersion test, and for evaluation of its phase transformation during the solidification process.

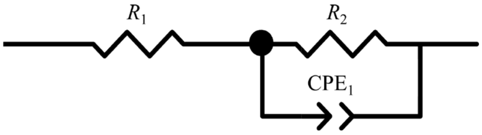

Fig. 7 Equivalent electrical circuit used for modeling EIS data

Table 2 Fitting parameters of EIS spectra

Sample	$R_1/(\Omega\cdot cm^2)$	$R_2/(\Omega\cdot cm^2)$	$CPE_1/(\Omega^{-1}\cdot cm^{-2}\cdot s^P)$	P
As-cast	7.26	60.78	1.10×10^{-4}	0.79
S150	8.06	173.60	4.41×10^{-5}	0.89
S160	8.13	190.00	4.81×10^{-5}	0.88
S170	8.78	181.30	1.93×10^{-5}	0.92

P is the dimensionless exponent of the CPE; A higher P (close to 1) indicates a more ideal capacitive behavior for that branch

3.2.2 Corrosion behavior

Immersion test was used to compare the corrosion degrees of the as-cast sample and the S160 sample, and OM images of the corrosion surfaces of the two samples are shown in Figs. 8 and 9, respectively. In the as-cast sample, at an immersion time of 4 h, pitting corrosion was evident on the surface in the form of shallow corrosion craters (marked by the red circle in Fig. 8(a)), and the sample exhibited a surface corrosion depth of 38.5 μm (Fig. 8(d)). Upon increasing the immersion time to 8 h, pitting corrosion was found to extend over the entire surface, and the depth of surface corrosion increased to 93.7 μm (Figs. 8(b) and (e)). Moreover, with an experimental time of 12 h, the degree of surface corrosion became severer, reaching a depth of 100.3 μm (Figs. 8(c) and (f)). Furthermore, Fig. 9 shows the corrosion morphologies of the S160 sample during the immersion. In this case, at an immersion time of 4 h, uniform surface corrosion was evident, with no obvious corrosion products being observed, and surface corrosion depth of 14.3 μm being recorded (Figs. 9(a) and (d)). Upon increasing the immersion time to 8 h, obvious pitting corrosion was observed (marked by the yellow circle in Fig. 9(b)), and the depth of surface corrosion increased slightly to 15.5 μm (Fig. 9(e)). After 12 h immersion, pitting became severer (Fig. 9(c)), and corrosion voids appeared in the

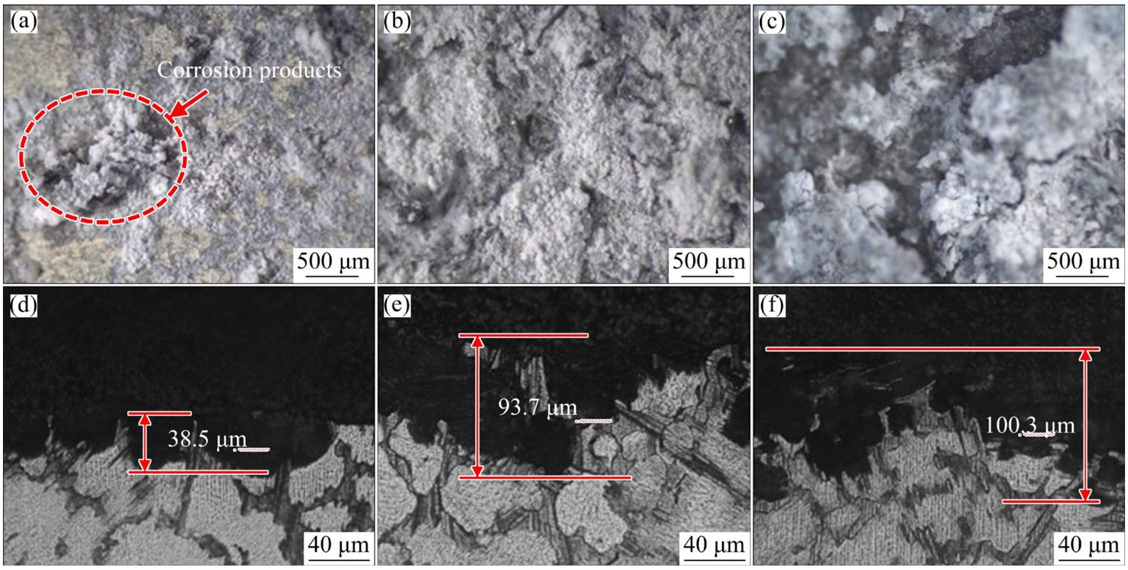

Fig. 8 OM images of as-cast sample immersed for different time: (a−c) Surface images for 4, 8, and 12 h immersion, respectively; (d−f) Cross-sectional images for 4, 8, and 12 h immersion, respectively

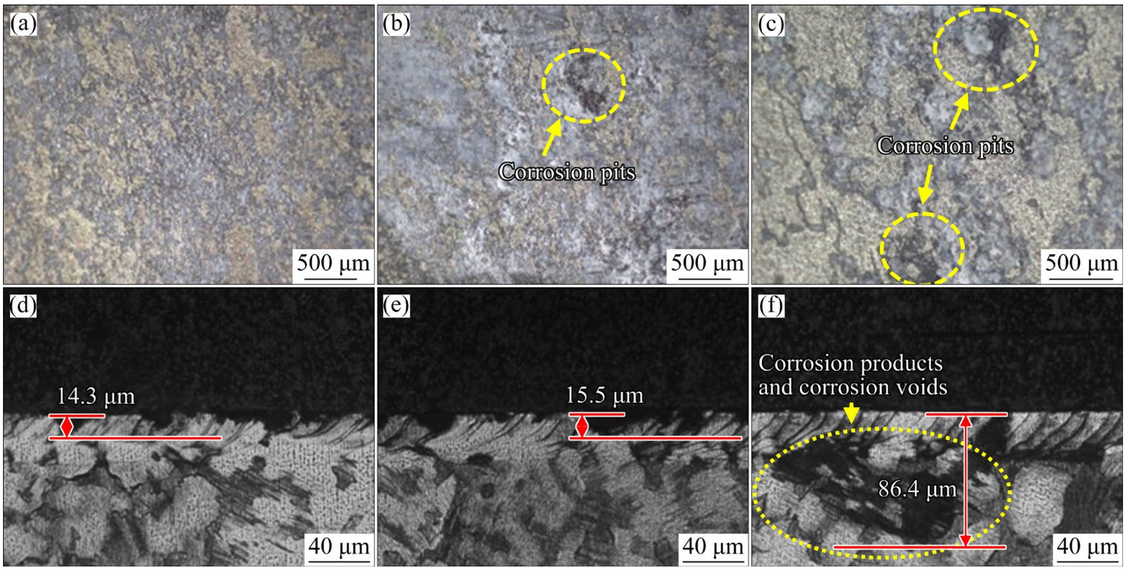

Fig. 9 OM images of S160 sample immersed for different time: (a−c) Surface images for 4, 8, and 12 h immersion, respectively; (d−f) Cross-sectional images for 4, 8, and 12 h immersion, respectively

matrix below the melted layer, giving a surface corrosion depth of 86.4 μm (Fig. 9(f)).

In terms of the corrosion behaviors of LPSO-containing Mg alloys, numerous experiments have been conducted to clarify the relationship between the LPSO phase and the degree of corrosion resistance. As previously reported, corrosion tended to arise preferentially at the interface between the LPSO phase and α-Mg, and gradually deepened along the edges of the LPSO phase [35,43,44]. Upon increasing the corrosion time, the α-Mg phase inside the grains was completely corroded, exposing the LPSO phase at the grain boundaries. The corrosion reactions taking place in the α-Mg matrix can be summarized as follows:

$$\mathrm{Mg}\rightarrow\mathrm{Mg}^{2+}+2\mathrm{e} \tag{3}$$

$$2\mathrm{H_2O}+2\mathrm{e}\rightarrow\mathrm{H_2}\uparrow+2\mathrm{OH}^- \tag{4}$$

$$\mathrm{Mg}^{2+}+2\mathrm{OH}^-\rightarrow\mathrm{Mg(OH)_2}\downarrow \tag{5}$$

According to Reactions (3)−(5), the corrosion products are $Mg(OH)_2$. The corresponding mass loss of the samples was recorded by removing the corrosion products, and the steady-state corrosion rate (CR, mm/a) was calculated using the mass loss method based on ASTM G31—72 standard, as defined in Eq. (6) [45]:

$$\mathrm{CR}=\frac{8.76\times10^{4}\Delta g}{At\rho} \tag{6}$$

where Δg is the mass loss (g), A is the sample surface area (cm^2), ρ is the alloy density ($\mathrm{g/cm}^3$), and t is the immersion time (h). The density of the alloy was taken as 2.06 $\mathrm{g/cm}^3$.

The corrosion rates recorded for the as-cast and S160 samples in a 3.5 wt.% NaCl solution are presented in Fig. 10, wherein it can be seen that throughout the immersion process, the corrosion rates of the as-cast samples exceeded those of the melted samples. Notably, the surfaces of the as-cast samples were unstable, leading to larger errors during immersion testing. In contrast, the surfaces of the melted samples were stable, resulting in smaller errors. Although the corrosion rates of the as-cast and laser-treated samples increased with increasing immersion time, their trends were different. More specifically, the corrosion rate of the as-cast sample initially increased because the sample surface became rough during the corrosion process, leading to an increased contact area between the corroding liquid and the sample surface. Upon reaching a corrosion time of 20 h, the surface roughness remained essentially unchanged, and the corrosion rate reached a plateau. In contrast, the corrosion rates of the laser-treated samples were initially stable, prior to rapidly increasing after 12 h of immersion. This initial stability was attributed to the laser-melted layer exhibiting considerable resistance to the external corrosive liquids in the early stages of corrosion. Subsequently, beyond an immersion period of 12 h, the corrosive liquids penetrated into the melted layer, leading to a marked increase in the corrosion rate.

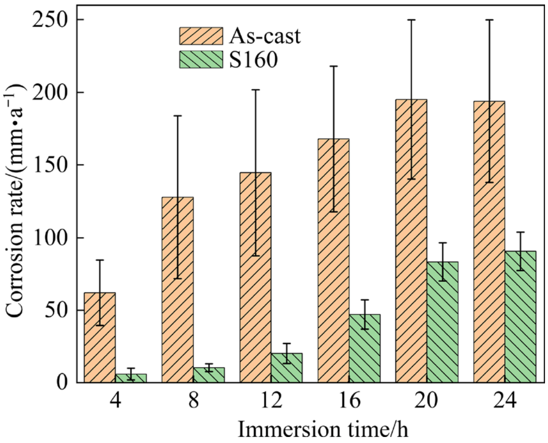

Fig. 10 Corrosion rates of as-cast and S160 samples after immersion in 3.5 wt.% NaCl solution for 4, 8, 12, 16, 20 and 24 h

3.3 Solidification structure and phase transformation

To further analyze the melted layer, inverse pole figure (IPF) and image quality (IQ) plots were employed to evaluate the cross-sectional microstructure of the S160 specimen. During LSM, the surface layer of the alloy melts and reaches a high temperature. Since cold steel clamps surround the alloy, the melted zone is subjected to a high cooling rate, and there is insufficient time for the heat-affected zone to form [46]. As shown in Fig. 11, the S160 sample can be divided into two regions (yellow dashed line), namely the melted region (I) and the matrix region (II). In the IPF (Fig. 11(a)), the maximum grain size is ~15 μm in Region I and ~300 μm in Region II, indicating that

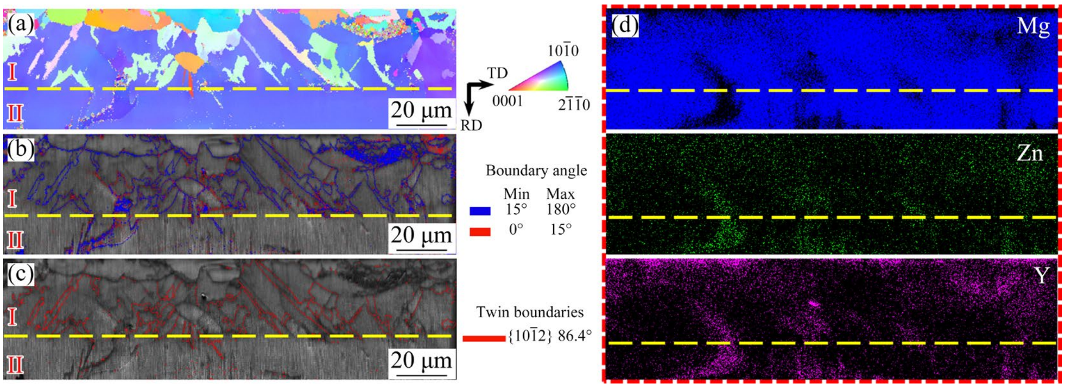

Fig. 11 Microstructure and elemental composition of cross-section of S160 sample: (a) IPF; (b) IQ plot of boundary rotation angle; (c) IQ plot of twin boundary; (d) EDS mappings

the grains are significantly refined after laser treatment. Additionally, lenticular grains with a thickness of ~1 μm and ultrafine-grained regions consisting of nanoscale grains (~200 nm) can be observed in the melted region. As shown in the IQ plot of the boundary rotation angle in Fig. 11(b), the Region I possesses a significantly greater number of high-angle grain boundaries (HAGBs, rotation angle >15°) than Region II, especially in the ultrafine-grained regions, indicating that there are more grains in the melted layer than in the matrix, i.e., the grains are refined. In addition, Fig. 11(c) presents an IQ plot that indicates the boundaries of the $\{10\bar{1}2\}$ twin. These boundaries coincide perfectly with the grain boundaries of the lenticular grains, confirming that they are indeed $\{10\bar{1}2\}$ twins. From the EDS mapping results presented in Fig. 11(d), it can be seen that Mg, Zn, and Y are more uniformly distributed on the cross-section of Region I than in Region II. This observation is consistent with the surface EDS mapping results presented in Fig. 3. However, areas with lower Mg contents and higher Zn and Y contents were also present. Thus, based on the distribution of the LPSO phase in the untreated sample, it is speculated that the original LPSO phase exists in these regions. Combined with the IPF shown in Fig. 11(a), it is apparent that the regions with reduced Mg contents and enriched Zn and Y contents coincide perfectly with the ultrafine-grained regions. Thus, during the melting and solidification processes, the LPSO phase region forms an ultrafine-grained region.

To further analyze the microstructure and phases in the melted layer, TEM test was conducted, as shown in Figs. 12−15. More specifically, Fig. 12(a) shows the bright-field (BF) TEM image of the melted layer, wherein the presence of large grains (~15 μm) and nearby small grains (~2 μm) is confirmed. The dominant feather of these grains is lamellar structures bound by nanoscale phases, as indicated by the arrows. The shapes of the large and small grains formed in the melted layer are irregular, as shown in Fig. 12(b). The insert gives the selected area electron diffraction (SAED) image of the framed area, revealing the $[2\bar{1}\bar{1}0]$ zone axis of the *α*-Mg phase. As shown in Fig. 12(c), a wedge-shaped grain is present in the melted layer,

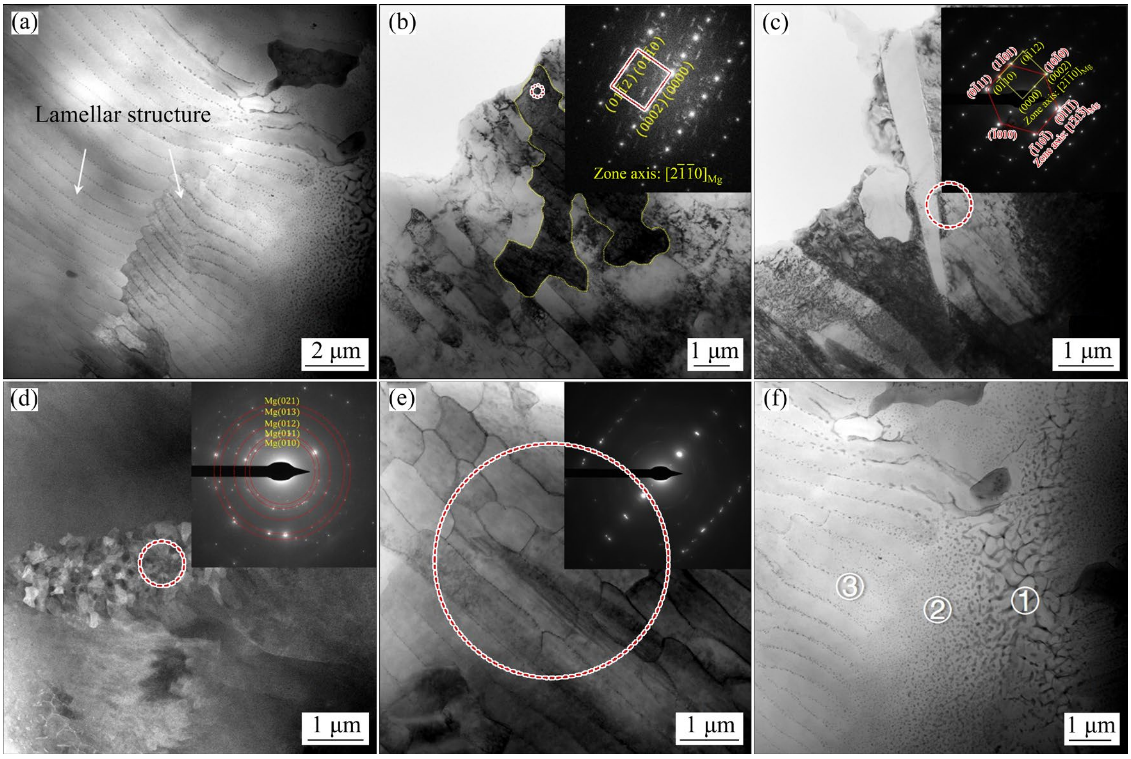

Fig. 12 TEM images of melted layer in S160 specimen: (a) BFTEM image of large and small grains; (b) BFTEM image of irregular shape of grains; (c) BFTEM image of wedge-shaped area; (d) DFTEM image of ultrafine grains; (e) BFTEM image of subgrains; (f) BFTEM image of different morphologies within large grains in (a) (The insert in each figure is SAED image of red circle)

which has no twinning orientation relationship with the Mg matrix, but has other orientation relationships. More specifically, as illustrated by the SAED image in the inset of Fig. 12(c), the orientation relationship between the wedge-shaped area and the Mg matrix is $[2\bar{1}\bar{1}0]_{\text{matrix}}//[1\bar{2}1\bar{3}]_{\text{wedge}}$. In addition to the morphologies shown in Figs. 12(a−c), ultrafine grains (~200 nm) were observed in the melted zone, as indicated by the dark-field (DF) TEM image in Fig. 12(d). These ultrafine grains are polycrystals, as confirmed by the SAED image, and they are consistent with the ultrafine-grained areas observed in the EBSD image (Fig. 11(a)). It is worth noting that $\{10\bar{1}2\}$ twins are not observed in the TEM sample, likely due to the sample preparation method, which only allows observation of the outermost layer of the sample after laser treatment. Figure 12(e) shows a BFTEM image of the subgrains ahead of the lamellar structures. Because the crystallographic orientation of these subgrains is consistent with the orientation of lamellar structures and the nanophase at the subgrain boundaries is the same to that bound the lamellar structures, these subgrains are not distinguished from the previously mentioned lamellar structures in the subsequent analysis. Figure 12(f) shows the magnified image of the three typical phases appearing within the large grains in Fig. 12(a), i.e., the network phase, the dispersed phase, and the streamlined dispersed phase, indicating by the markers "①", "②", and "③", respectively.

The nanoscale phases with different morphologies precipitated during the solidification process were analyzed in additional detail, as shown in Figs. 13−15. More specifically, Fig. 13 shows the crystal structure and composition of the network phase. As can be seen from the BFTEM image and element distribution map of the network phase (A) given in Fig. 13(a), this phase is enriched

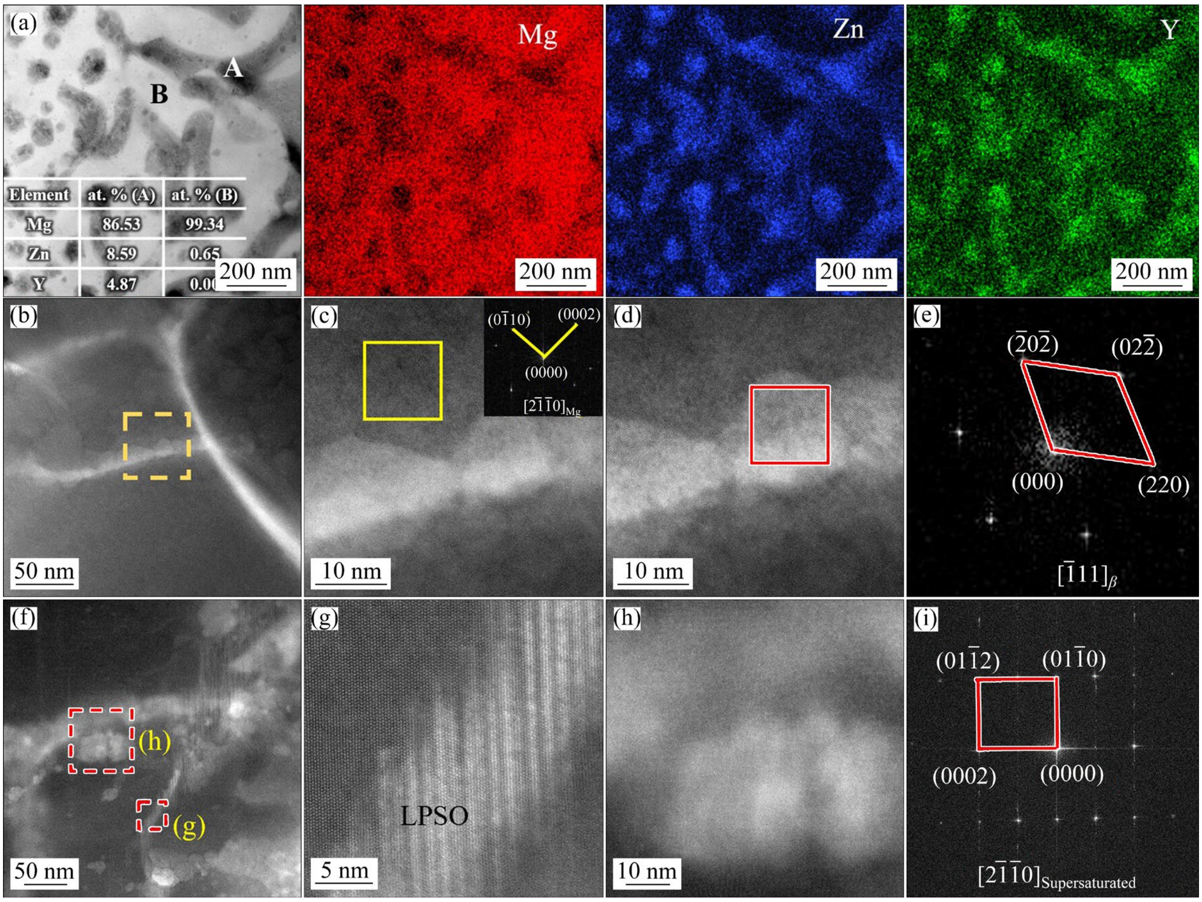

Element	at. % (A)	at. % (B)
Mg	86.53	99.34
Zn	8.59	0.65
Y	4.87	0.0

Fig. 13 TEM images and elemental analysis results of network phase in melted layer of S160 sample: (a) BFTEM image and element distribution map; (b) STEM image; (c, d) Atomic-scale views of dotted framed area in (b) showing clear lattice of Mg matrix and network phase, respectively; (e) FFT image of red-framed area in (d); (f) STEM image showing supersaturated α-Mg and LPSO phases nearby some β phases; (g, h) Enlarged view of red frame areas in (f) showing LPSO and α-Mg phases, respectively; (i) FFT image corresponding to (h)

with Zn and Y elements (c.f., the α-Mg matrix, B). Since its morphology resembles the β-$(Mg,Zn)_3Gd$ phase observed during laser additive manufacturing of the Mg−Zn−Gd alloy [47,48], it is speculated that this phase is the β-$(Mg,Zn)_3Y$ phase. Figure 13(b) shows a STEM image of the network phase, while Figs. 13(c) and (d) show magnified images of the area indicated by the dashed box in Fig. 13(a). Because of different thicknesses of the Mg matrix and the network phase, they cannot be focused on simultaneously. Therefore, two images were captured at the same position: Fig. 13(c) shows the clear lattice of the Mg matrix, whereas Fig. 13(d) shows the clear lattice of the network phase. In addition, Fig. 13(e) shows a fast Fourier transform (FFT) image of the area enclosed by the red frame in Fig. 13(d). Combining Figs. 13(c−e), it is evidently proven that the network phase is indeed a β phase possessing a face centered cubic lattice structure. The lattice constant of the β phase is calculated to be 0.72 nm, and it is found that the β phase has a good orientation relationship with the Mg matrix, i.e., $(01\bar{1})_\beta // (0001)_{Mg}$ and $[\bar{1}11]_\beta // [2\bar{1}\bar{1}0]_{Mg}$. Additionally, it is noteworthy that some irregularly shaped supersaturated α-Mg phases and LPSO phases with a width of several tens of nanometers are observed in certain areas around the network β phase using STEM, as shown in Fig. 13(f). The atomic structures of the LPSO phase and the supersaturated α-Mg phase are presented in Figs. 13(g) and (h), respectively, while Fig. 13(i) displays the FFT image corresponding to Fig. 13(h). However, the reasons for the formation of these phases require further investigation.

Figure 14 shows the TEM images recorded for the dispersed phase. More specifically, Fig. 14(a) presents the BFTEM image and point scan results for the dispersed phase (C), demonstrating that it is enriched with Zn and Y compared to the Mg matrix. The enlarged view of the dispersed phase is shown in Fig. 14(b). Figures 14(c) and (d) show high-resolution TEM and STEM images of dispersed phase along the [0001] zone axis of the Mg matrix,

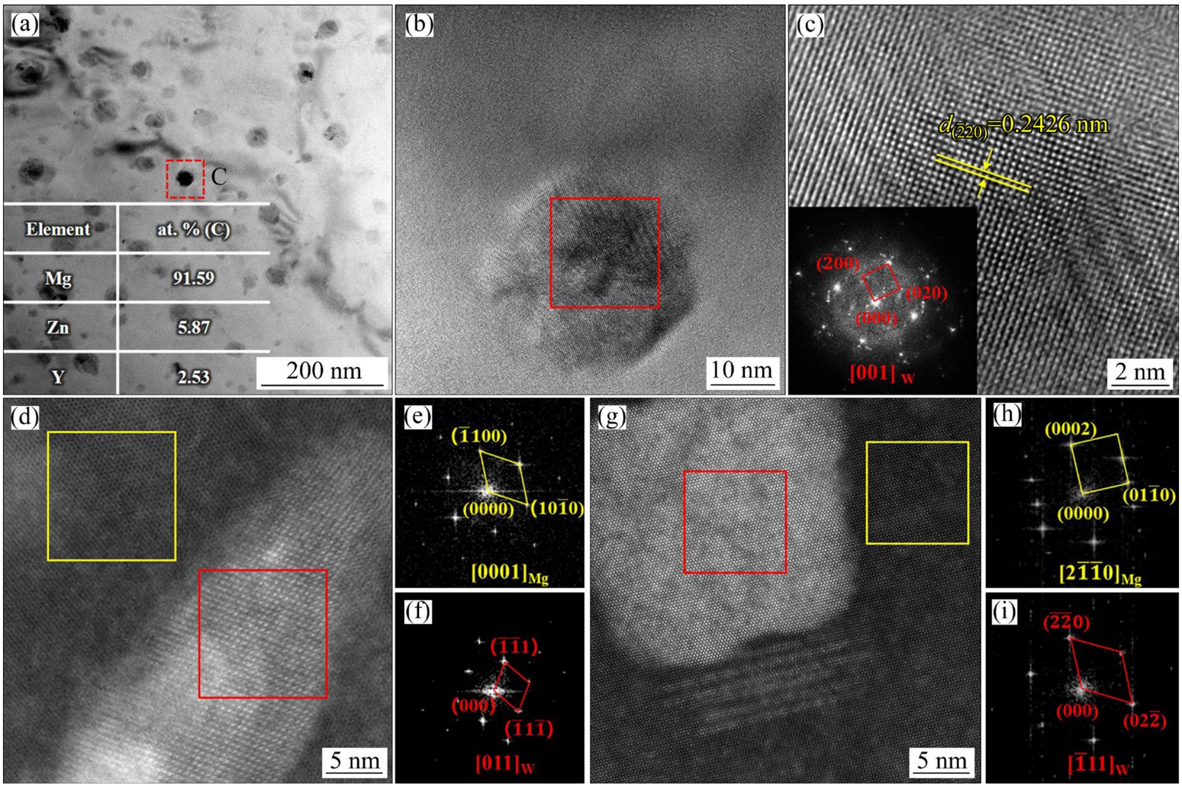

Fig. 14 TEM images of dispersed phase (*W* phase) in melted layer of S160 sample: (a) BFTEM image and point scan results of *W* phase; (b) Enlarged view of red-framed area in (a); (c) High-resolution image of red-framed area in (b), wherein, insert is FFT image corresponding to (c); (d) Atomic-scale STEM image of *W* phase along [0001] zone axis of Mg matrix; (e, f) FFT images corresponding to yellow- and red-framed areas in (d), respectively; (g) Atomic-scale STEM image of *W* phase along $[2\bar{1}\bar{1}0]$ zone axis of Mg matrix; (h, i) FFT images corresponding to yellow- and red-framed areas in (g), respectively

respectively. Furthermore, Figs. 14(e) and (f) show the corresponding FFT images of the yellow- and red-framed areas in Fig. 14(d), respectively. Figure 14(g) shows an atomic-scale STEM image of the dispersed phase along the $[2\bar{1}\bar{1}0]$ zone axis of the Mg matrix, while Figs. 14(h) and (i) show the FFT images corresponding to the yellow- and red-framed areas in Fig. 14(g), respectively. It is revealed that the dispersed phase is the *W* phase ($Mg_3Y_2Zn_3$), with a lattice constant of 0.69 nm. The orientation relationship between the *W* phase and the Mg matrix is defined as $(\bar{1}\bar{1}0)_W//(0001)_{Mg}$ and $[\bar{1}11]_W//[2\bar{1}\bar{1}0]_{Mg}$.

Figure 15 shows the TEM images of the streamlined dispersed phase, wherein Fig. 15(a) presents the BFTEM image and point scan results for this phase. It is confirmed that the streamlined dispersed phase (D) is enriched with Zn and Y elements. In addition, Figs. 15(b) and (c) show the high-resolution images of the phase along the $[\bar{1}01\bar{1}]$ zone axis of the Mg matrix and its corresponding FFT image, respectively, while Fig. 15(d) shows an atomic-scale STEM image of the phase along the $[2\bar{1}\bar{1}0]$ zone axis of the Mg matrix. Figures 15(e) and (f) show FFT images corresponding to the yellow- and red-framed areas in Fig. 15(d), respectively, while Fig. 15(g) shows an elemental distribution maps of the streamlined dispersed phase corresponding to the area presented in Fig. 15(a). From these figures, it is determined that the streamlined dispersed phase is the supersaturated α-Mg phase, which possesses completely coherent interfaces with the Mg matrix. The orientation relationship between the supersaturated α-Mg phase and the Mg matrix is defined as $(0001)_{Supersaturated}//(0001)_{Mg}$ and $[2\bar{1}\bar{1}0]_{Supersaturated}//[2\bar{1}\bar{1}0]_{Mg}$. Additionally, a number of stacking faults (SF) enriched with solute elements are detected around the supersaturated α-Mg phases, as shown by the arrows in Fig. 15(d).

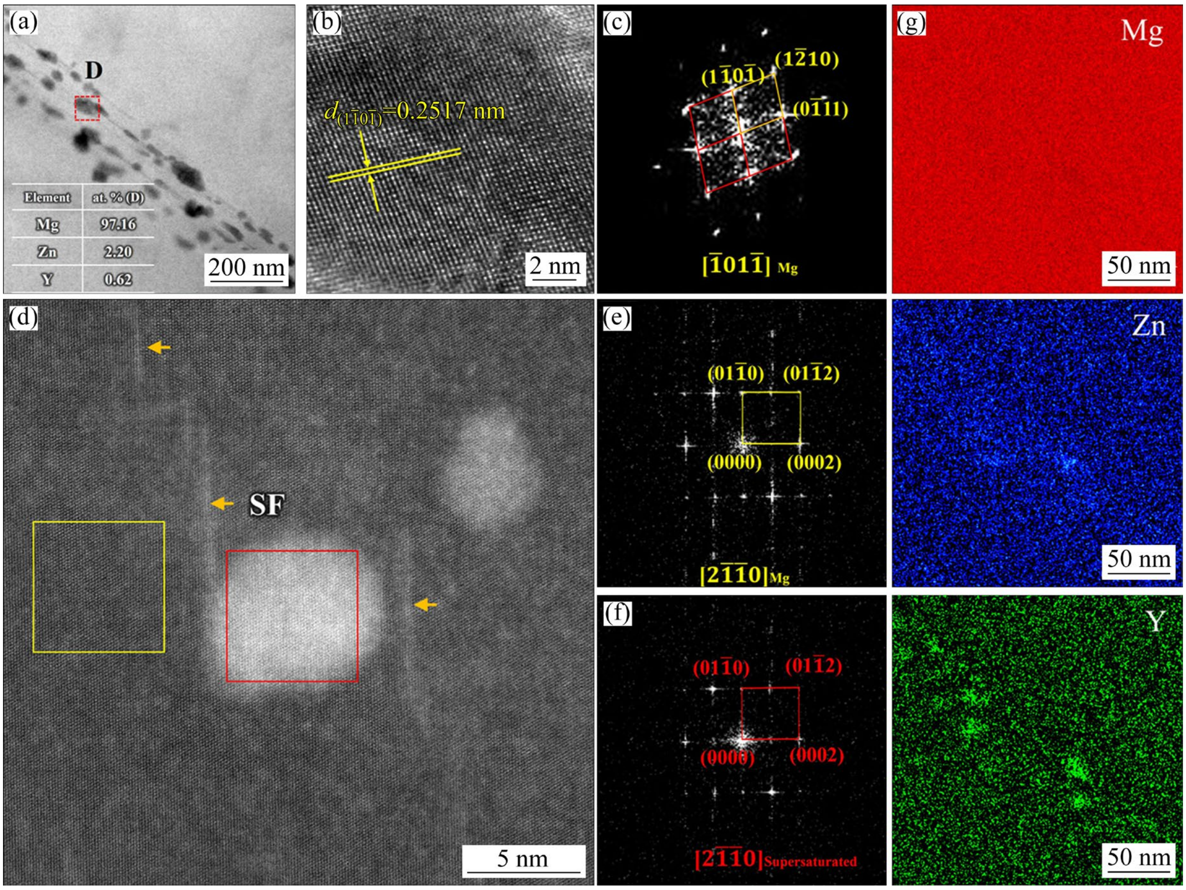

Fig. 15 TEM images of streamlined dispersed phase (supersaturated α-Mg phase); (a) BFTEM image and point scan results; (b) High-resolution image of red-framed area in (a); (c) FFT image corresponding to (b); (d) Atomic-scale STEM image along $[2\bar{1}\bar{1}0]$ zone axis of Mg matrix; (e, f) FFT images corresponding to yellow- and red-framed areas in (d), respectively; (g) Elemental distribution maps corresponding to red-framed area in (a)

4 Discussion

4.1 Formation of irregular grains and intracrystalline secondary phases

During LSM, the alloy absorbs laser energy and undergoes melting. After the melted layer solidifies, the Mg grains are refined into grains with irregular shapes, while the LPSO phase transforms into ultrafine *α*-Mg grains. This can be attributed to the fact that the extremely rapid cooling rate and inhomogeneity of the solutes can result in the instability of the cooling process. In addition, the multidirectional heat flow, the curved surface of the isotherms, and the non-planar nature of the solid–liquid interface lead to instability at this interface. Since the shape of the solid–liquid interface controls microstructural development [49], the shape of the grains generated in the melted layer is irregular. Furthermore, the shape of the twins is also affected, some of which do not exhibit a standard lens shape; the twin boundaries are always uneven. Considering that rapid cooling conditions can induce local thermal stress, this may account for the observed structures in which small grains surround large grains. Figure 11(d) shows that the melted region rich in solute elements is the area where the original LPSO phase is located. Owing to the extremely fast cooling rate and the effects of the Zn and Y solutes in local areas, various grain refinement mechanisms may occur, such as the promotion of nucleation and the inhibition of grain growth. These mechanisms work together to significantly reduce the grain size, ultimately leading to the formation of ultrafine grains.

Cooling under unstable conditions produces precipitates with various morphologies and lamellar structures in the grains. Figures 16(a) and (b) illustrate the microstructures of the alloy before LSM and the molten pool after LSM, respectively. According to the Mg−Zn−Y ternary phase diagram, during the solidification process, the crystallization temperature of the *β*-$(Mg,Zn)_3Y$ eutectic phase is higher than that of the *W* phase [50]. Therefore, the *β* eutectic phase will precipitate first from the liquid, as presented in Fig. 16(c). At a slower cooling rate, the *β* eutectic phase has sufficient time to grow and generate a wide network morphology [48]. However, under rapid cooling, the formation time of the *β* eutectic phase is limited, a network morphology exhibits a small range, and a reduced volume is formed, as shown in Fig. 16(d). Upon decreasing the temperature to the crystallization temperature of the *W* phase, the *W* phase begins to precipitate, as can be seen from Fig. 16(d). Similarly to the *β* phase, in the case of a slow cooling, the *W* phase has sufficient time to form a large and extensive reticular morphology [51]. Under high cooling rate, the growth of the *W* phase is inhibited, resulting in the formation of small unexpanded *W* phase particles, as shown in Fig. 16(e). Subsequently, lamellae grew from the *W* phase zone are formed on the basal plane of the Mg matrix, as demonstrated by the SAED pattern and

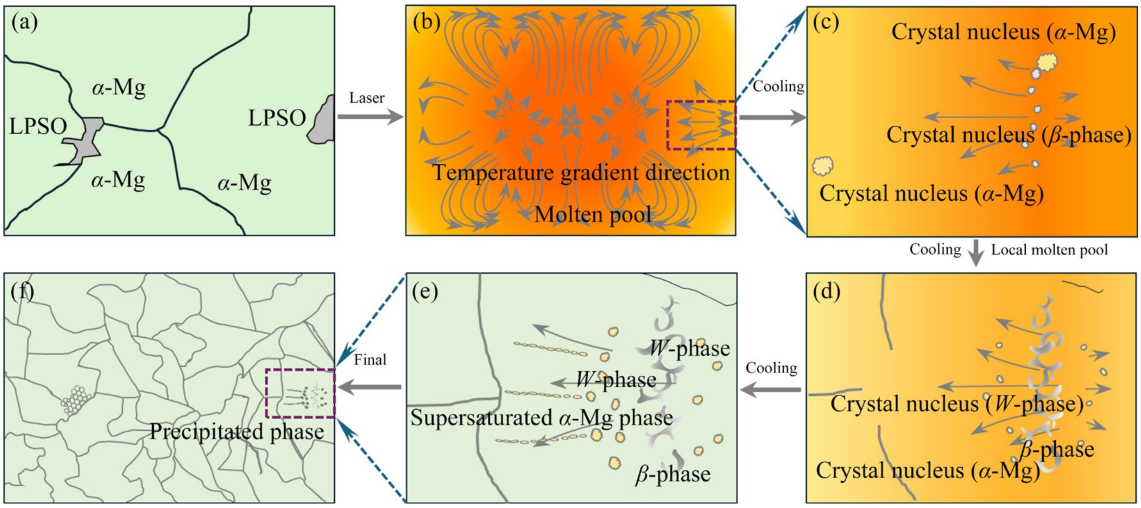

Fig. 16 LSM schematics of melted layer on surface of Mg−Zn−Y alloy: (a) Before LSM; (b) Temperature gradient in molten pool; (c) *β*-phase precipitation; (d) *W*-phase precipitation; (e) Lamellar structure generation; (f) Final microstructure after LSM (The arrow directions in (c) and (d) indicate solidification directions)

TEM image presented in Fig. 12. It is reported that slower growth rates in the off-basal plane compared to the basal plane generate parallel dendritic grains along the basal plane [52]. In addition, it is observed that the supersaturated *α*-Mg phases create boundaries between the lamellae. Therefore, while the dendrites grow from the *W*-phase zone and lamellae are formed, the limited growth between these lamellae generates an interdendritic liquid enriched in the solute elements, mainly Zn and Y. When the temperature is decreased further, the Zn/Y-enriched liquid solidifies and the boundaries are formed. In this case, the supersaturated *α*-Mg phase does not form within the lamellae, due to different growth rates in the on- and off-basal plane directions, the low solute content of the alloy, and the rapid solidification taking place during the LSM process.

4.2 Mechanisms responsible for enhanced corrosion resistance

The corrosion mechanisms of the alloy before and after LSM are shown in Figs. 17(a) and (b), respectively. It can be seen from Fig. 17(a) that during the corrosion process, the LPSO phase acted as the cathode and the Mg matrix served as the anode. As previously reported, micro-galvanic acceleration generally depended on the area ratio of the cathode to the anode, wherein a larger ratio produced severer micro-galvanic corrosion [53,54]. However, the alloy exhibited its highest corrosion resistance when the volume fraction of the LPSO phase is ~50%. If the volume fraction of the LPSO phase is greater or less than 50%, the corrosion resistance of the alloy decreases [55]. Based on measurements performed using ImageJ software, the area fraction of the LPSO phase in the as-cast alloy was determined to be ~25%. Because of the low area ratio of the LPSO phase, severe localized corrosion of the *α*-Mg anodic phase occurred. Following LSM, the discontinuous LPSO blocks present on the surface of the Mg−Zn−Y alloy disappeared. In addition, the interface that originally existed on the surface between the large LPSO phase and the *α*-Mg matrix disappeared, greatly reducing the degree of corrosion (Fig. 17(b)). However, small phases still precipitated in the laser-melted layer. Although such precipitates tended to be less reactive than the *α*-Mg matrix and acted as cathodes to accelerate the corrosion of Mg matrix [47], it was found that LSM treatment led to a significantly lower corrosion rate than that of the as-cast alloy.

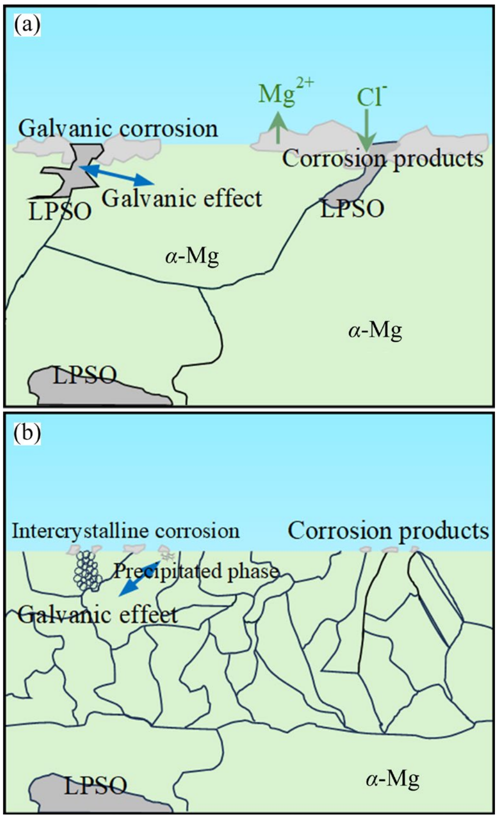

Fig. 17 Schematic diagrams of corrosion mechanisms of different samples: (a) As-cast; (b) S160

The grain size is also known to affect the corrosion resistance properties of Mg alloys. In the current system, the corrosion mechanism of the as-cast alloy containing large grains was dominated by micro-galvanic coupling between the *α*-Mg and LPSO phases, and it was found that grain refinement reduced the corrosion rate of the Mg alloy. This can be attributed to two main mechanisms. Firstly, grain refinement accelerated the formation of the surface magnesium hydroxide layer to reduce the corrosion rate [56], and secondly, a large fraction of the grain boundaries relieved the stress between the corrosion layer and the matrix, thereby reducing the tendency of the protective layer to crack [57]. Therefore, the laser-melted layer promoted the dissolution of the LPSO phase and smaller-sized grains, and precipitated phases are generated, which reduced the corrosion micro-current and enhanced the corrosion resistance [58]. However, when the protective magnesium hydroxide film ruptured, the corrosive solution continued to corrode the metal along the film rupture point. This can result in intergranular corrosion, causing local areas to corrode downwards along the grain boundaries and penetrate into the melted layer, as shown in Fig. 9(f). Nevertheless, the melted layer was found to exhibit relatively uniform corrosion, in addition to a lower corrosion rate than the untreated alloy.

5 Conclusions

(1) The corrosion resistance of the Mg−Zn−Y alloy was significantly improved after LSM treatment at 150−170 W, with the optimal results being obtained at 160 W. Following LSM treatment, a 15−30 μm layer was detected on the alloy surface, containing a uniform distribution of Mg, Zn, and Y.

(2) Rapid solidification during the LSM process was found to generate a significant reduction in the grain size, along with an uneven grain size distribution (2−15 μm) in the melted layer. Rapid solidification also induced the production of ultrafine grains from the original LPSO phase and 1 μm-thick twins.

(3) It was deduced that the refined irregularly shaped grains mainly consisted of three adjacent zones, namely, the β eutectic phase zone, the W phase zone, and the lamellar structure zone. Importantly, the disappearance of large primary batteries and additional grain refinement led to an enhanced corrosion resistance for this alloy.

CRediT authorship contribution statement

Zhen-zhen PENG: Conceptualization, Methodology, Validation, Formal analysis, Investigation, Data curation, Writing − Original draft, Writing − Review & editing, Funding acquisition; **Min-heng XU:** Methodology, Validation, Investigation, Writing − Review & editing; **Xiao-hong SHAO:** Writing − Review & editing, Funding acquisition, Project administration, Supervision; **Xiao YANG**: Data curation, Formal analysis; **Heng-hu ZHAO:** Data curation, Investigation, Validation; **Zhi-min LIANG:** Writing − Review & editing, Project administration, Supervision; **Dian-long WANG:** Funding acquisition, Formal analysis; **Ying LIU**: Software.

Declaration of competing interest

The authors declare that they have no known competing financial interests or personal relationships that could have appeared to influence the work reported in this paper.

Acknowledgments

This work was supported by the National Natural Science Foundation of China (Nos. 52101015, 52171021), the National Key R&D Program of China (No. 2021YFA1600704), the Science and Technology Research Project of Colleges and Universities in Hebei Province, China (No. BJK2022020), and the Natural Science Foundation of Hebei Province, China (No. E2022208070).

References

[1] NIE J F, ZHU Y M, LIU J Z, FANG X Y. Periodic segregation of solute atoms in fully coherent twin boundaries [J]. Science, 2013, 340: 957−960.

[2] KUMAR D, PHANDEN R K, THAKUR L. A review on environment friendly and lightweight magnesium-based metal matrix composites and alloys [J]. Materials Today: Proceedings, 2021, 38: 359−364.

[3] CHEN Lian-yi, XU Jia-quan, CHOI H, POZUELO M, MA Xiao-long, BHOWMICK S, YANG Jenn-ming, MATHAUDHU S, LI Xiao-chun. Processing and properties of magnesium containing a dense uniform dispersion of nanoparticles [J]. Nature, 2015, 528: 539−543.

[4] LIU Xuan, ZHANG Zhi-qiang, LE Qi-chi, BAO Lei. Effects of Nd/Gd value on the microstructures and mechanical properties of Mg−Gd−Y−Nd−Zr alloys [J]. Journal of Magnesium and Alloys, 2016, 4: 214−219.

[5] LIU Ke, LOU Feng, FU Jun-jian, YU Zi-jian, LI Shu-bo, WANG Zhao-hui, DU Xian, DU Wen-bo. Microstructure and corrosion behaviors of as-rolled Mg−Zn−Er alloy sheets [J]. Transactions of Nonferrous Metals Society of China, 2022, 32: 1881−1895.

[6] QIU Wei, LI Ya-wen, HUANG Gang, CHEN Jian, REN Yan-jie, HUANG Wei-ying, CHEN Wei, WU Tang-qing, YAO Mao-hai, XIONG Ai-hu. Corrosion behavior of as-cast AZ91 magnesium alloy with VN particle additions in NaCl solution [J]. Transactions of Nonferrous Metals Society of China, 2023, 33: 1398−1410.

[7] XIA Xiang-sheng, ZHANG Kui, MA Ming-long, LI Ting. Microstructures and strengthening mechanisms of Mg−8.2Gd−4.6Y−1.5Zn−0.4Zr alloy containing LPSO, β' and γ type phases [J]. Journal of Rare Earths, 2020, 38: 1119−1125.

[8] DING Shuai-jun, CAI Xue-cheng, LI Zhong-jie, XU Li-dong, WEN Kang-kang, SONG Jian, CUI Hong-wei, YU Hui, SHEN Tong-de. Achieving ultra-strong Mg alloys via a novel hierarchical long-period stacking ordered architecture [J]. Journal of Alloys and Compounds, 2021, 870: 159343.

[9] WANG Dan, LIU Shu-juan, WU Rui-zhi, ZHANG Shun, WANG Yang, WU Hua-jie, ZHANG Jing-huai, HOU Le-gan. Synergistically improved damping, elastic modulus and

mechanical properties of rolled Mg−8Li−4Y−2Er−2Zn−0.6Zr alloy with twins and long-period stacking ordered phase [J]. Journal of Alloys and Compounds, 2021, 881: 160663.

[10] JIN Xue-ze, XU Wen-chen, YANG Zhong-ze, YUAN Can, SHAN De-bin, TENG Bu-gang, JIN Bo-cheng. Analysis of abnormal texture formation and strengthening mechanism in an extruded Mg−Gd−Y−Zn−Zr alloy [J]. Journal of Materials Science & Technology, 2020, 45: 133−145.

[11] XU Dao-kui, HAN En-hou, XU Yong-bo. Effect of long-period stacking ordered phase on microstructure, mechanical property and corrosion resistance of Mg alloys: A review [J]. Progress in Natural Science: Materials International, 2016, 26: 117−128.

[12] ZHAO Ming-chun, LIU Ming, SONG Guang-ling, ATRENS A. Influence of the *β*-phase morphology on the corrosion of the Mg alloy AZ91 [J]. Corrosion Science, 2008, 50: 1939−1953.

[13] CIHOVA M, SCHMUTZ P, SCHÄUBLIN R, LÖFFLER J F. Biocorrosion zoomed In: Evidence for dealloying of nanometric intermetallic particles in magnesium alloys [J]. Advanced Materials, 2019, 31: e1903080.

[14] ZENG Zhuo-ran, STANFORD N, DAVIES C H J, NIE Jian-feng, BIRBILIS N. Magnesium extrusion alloys: A review of developments and prospects [J]. International Materials Reviews, 2019, 64: 27−62.

[15] ESMAILY M, SVENSSON J E, FAJARDO S, BIRBILIS N, FRANKEL G S, VIRTANEN S, ARRABAL R, THOMAS S, JOHANSSON L G. Fundamentals and advances in magnesium alloy corrosion [J]. Progress in Materials Science, 2017, 89: 92−193.

[16] RAKESH K R, BONTHA S, RAMESH M R, DAS M, BALLA V K. Laser surface melting of Mg−Zn−Dy alloy for better wettability and corrosion resistance for biodegradable implant applications [J]. Applied Surface Science, 2019, 480: 70−82.

[17] MAJUMDAR J D, GALUN R, MORDIKE B L, MANNA I. Effect of laser surface melting on corrosion and wear resistance of a commercial magnesium alloy [J]. Materials Science and Engineering: A, 2003, 361: 119−129.

[18] DELGADO M C, GARCÍA-GALVAN F R, LLORENTE I, PÉREZ P, ADEVA P, FELIU S. Influence of aluminium enrichment in the near-surface region of commercial twin-roll cast AZ31 alloys on their corrosion behaviour [J]. Corrosion Science, 2017, 123: 182−196.

[19] YANG Guang-zheng, YANG Hua-wei, SHI Lei, WANG Tao-lei, ZHOU Wu-chao, ZHOU Tian, HAN Wei, ZHANG Zhi-yuan, LU Wei, HU Jing-zhou. Enhancing corrosion resistance, osteoinduction, and antibacterial properties by Zn/Sr additional surface modification of magnesium alloy [J]. ACS Biomaterials Science & Engineering, 2018, 4: 4289−4298.

[20] SANKARA NARAYANAN T S N, PARK I S, LEE M H. Strategies to improve the corrosion resistance of microarc oxidation (MAO) coated magnesium alloys for degradable implants: Prospects and challenges [J]. Progress in Materials Science, 2014, 60: 1−71.

[21] YANG Chao, CUI Sui-han, FU R K Y, SHENG Li-yuan, WEN Min, XU Dao-kui, ZHAO Ying, ZHENG Yu-feng, CHU P K, WU Zhong-zhen. Optimization of the in vitro biodegradability, cytocompatibility, and wear resistance of the AZ31B alloy by micro-arc oxidation coatings doped with zinc phosphate [J]. Journal of Materials Science & Technology, 2024, 179: 224−239.

[22] LIU Xiao-he, LIU Lei, DONG Shuai, CHEN Xiao-bo, DONG Jie. Towards dense corrosion-resistant plasma electrolytic oxidation coating on Mg−Gd−Y−Zr alloy by using ultra-high frequency pulse current [J]. Surface and Coatings Technology, 2022, 447: 128881.

[23] XIE Jin-shu, ZHANG Jing-huai, YOU Zi-hao, LIU Shu-juan, GUAN Kai, WU Rui-zhi, WANG Jun, FENG Jing. Towards developing Mg alloys with simultaneously improved strength and corrosion resistance via RE alloying [J]. Journal of Magnesium and Alloys, 2021, 9: 41−56.

[24] LIU Jin-ge, YIN Bang-zhao, SONG Fei, LIU Bing-chuan, PENG Bo, WEN Peng, TIAN Yun, ZHENG Yu-feng, MA Xiao-lin, WANG Cai-mei. Improving corrosion resistance of additively manufactured WE43 magnesium alloy by high temperature oxidation for biodegradable applications [J]. Journal of Magnesium and Alloys, 2024, 12: 940−953.

[25] RAKOCH A G, MONAKHOVA E P, KHABIBULLINA Z V, SERDECHNOVA M, BLAWERT C, ZHELUDKEVICH M L, GLADKOVA A A. Plasma electrolytic oxidation of AZ31 and AZ91 magnesium alloys: Comparison of coatings formation mechanism [J]. Journal of Magnesium and Alloys, 2020, 8: 587−600.

[26] ZENG Si-qi, TIAN Jing-jing, HU Shu-bing, XIAO Ming, PENG Bo. Effect of laser surface melting on microstructure evolution and cavitation behavior of nickel aluminum bronze [J]. Transactions of Nonferrous Metals Society of China, 2023, 33: 2090−2109.

[27] GRAY J E, LUAN B L. Protective coatings on magnesium and its alloys: A critical review [J]. Journal of Alloys and Compounds, 2002, 336: 88−113.

[28] JANA S, OLSZTA M, EDWARDS D, ENGELHARD M, SAMANTA A, DING H T, MURKUTE P, ISGOR O B, ROHATGI A. Microstructural basis for improved corrosion resistance of laser surface processed AZ31 Mg alloy [J]. Corrosion Science, 2021, 191: 109707.

[29] LIN Peng-yu, GUO Yun-ting, ZHANG Zhi-hui, WANG Qing, KANG Zhong-xiong, YANG Hong-xiu, REN Lu-quan. Analysis of microstructure, treatment pattern, and corrosion behaviour of AZ91D magnesium alloy processed by selective laser surface remelting [J]. Journal of Materials Research and Technology, 2022, 21: 1293−1306.

[30] LIU Can-can, LIANG Jun, ZHOU Jian-song, WANG Ling-qian, LI Qing-biao. Effect of laser surface melting on microstructure and corrosion characteristics of AM60B magnesium alloy [J]. Applied Surface Science, 2015, 343: 133−140.

[31] LIU Can-can, LI Qing-biao, LIANG Jun, ZHOU Jian-song, WANG Ling-qian. Microstructure and corrosion behaviour

of laser surface melting treated WE43 magnesium alloy [J]. RSC Advances, 2016, 6: 30642−30651.

[32] LIAO Hong-xin, KIM J, LEE T, SONG Jiang-feng, PENG Jian, JIANG Bin, PAN Fu-sheng. Effect of heat treatment on LPSO morphology and mechanical properties of Mg−Zn−Y−Gd alloys [J]. Journal of Magnesium and Alloys, 2020, 8: 1120−1127.

[33] HAGIHARA K, UEYAMA R, YAMASAKI M, KAWAMURA Y, NAKANO T. Surprising increase in yield stress of Mg single crystal using long-period stacking ordered nanoplates [J]. Acta Materialia, 2021, 209: 116797.

[34] HAGIHARA K, LI Z X, YAMASAKI M, KAWAMURA Y, NAKANO T. Strengthening mechanisms acting in extruded Mg-based long-period stacking ordered (LPSO)- phase alloys [J]. Acta Materialia, 2019, 163: 226−239.

[35] XIE Jin-shu, ZHANG Jing-huai, ZHANG Zhi, YANG Qiang, GUAN Kai, HE Yu-ying, WANG Ru, ZHANG Hao, QIU Xin, WU Rui-zhi. New insights on the different corrosion mechanisms of Mg alloys with solute-enriched stacking faults or long period stacking ordered phase [J]. Corrosion Science, 2022, 198: 110163.

[36] YIN Si-qi, DUAN Wen-chao, LIU Wen-hong, WU Liang, YU Jia-min, ZHAO Zi-long, LIU Min, WANG Ping, CUI Jian-zhong, ZHANG Zhi-qiang. Influence of specific second phases on corrosion behaviors of Mg−Zn−Gd−Zr alloys [J]. Corrosion Science, 2020, 166: 108419.

[37] LI Chuan-qiang, XU Dao-kui, ZENG Zhuo-ran, WANG Bao-jie, SHENG Li-yuan, CHEN Xiao-bo, HAN En-hou. Effect of volume fraction of LPSO phases on corrosion and mechanical properties of Mg−Zn−Y alloys [J]. Materials & Design, 2017, 121: 430−441.

[38] PANG Meng-yao, ZHONG Tao, JIN Si-yuan, MA Xiao-chun, WU Rui-zhi, HOU Le-gan, TASHLYKOVA-BUSHKEVICH I I, KRIT B, ZHANG Jing-huai. Tailoring the degradation rate of magnesium−lithium alloy with alloying elements of gadolinium and nickel [J]. Journal of Alloys and Compounds, 2024, 976: 173115.

[39] XIE Jin-shu, ZHANG Jing-huai, ZHANG Zhi, YU Zi-jian, XU Zhi-hao, WANG Ru, FANG Da-qing, ZHANG Xiao-bo, ZHANG Xiao-ru, WU Rui-zhi. Corrosion mechanism of Mg alloys involving elongated long-period stacking ordered phase and intragranular lamellar structure [J]. Journal of Materials Science & Technology, 2023, 151: 190−203.

[40] XU Xiao-fang, YANG Xiao-han, LI Jing-bo, PAN Sen, BI Yong, GAO Yong-feng. Influence of laser energy distribution on laser surface microstructure processing [J]. Optik, 2019, 199: 163244.

[41] LIU Xi-qin, WU Ya-jie, LIU Zi-li, LU Cheng, XIE Huan-jian, LI Jian. Thermal and electrical conductivity of as-cast Mg−4Y−xZn alloys [J]. Materials Research Express, 2018, 5: 066532.

[42] FAJARDO S, MIGUÉLEZ L, ARENAS M A, de DAMBORENEA J, LLORENTE I, FELIU S. Corrosion resistance of pulsed laser modified AZ31 Mg alloy surfaces [J]. Journal of Magnesium and Alloys, 2022, 10: 756−768.

[43] XI Guo-qiang, ZHAO Xu-han, MA Yan-long, MOU Yu, XIONG Ju, MA Kai, WANG Jing-feng. Comparative study on corrosion behavior and mechanism of as-cast Mg−Zn−Y and Mg−Zn−Gd alloys [J]. Acta Metallurgica Sinica (English Letters), 2022, 36: 310−322.

[44] XU Li-dong, DING Shuai-jun, CAI Xue-cheng, WU Yun, LI Zhong-jie, WEN Kang-kang, XIN Sheng-wei, SUN Bao-run, HUANG Ming-xin, SHEN Tong-de. Unveiling initial oxidation behavior of Mg−Y−Zn long-period stacking ordered (LPSO) phase [J]. Corrosion Science, 2022, 208: 110624.

[45] YIN Si-qi, DUAN Wen-chao, LIU Wen-hong, WU Liang, BAO Jia-xin, YU Jia-min, LI Liang, ZHAO Zhong, CUI Jian-zhong, ZHANG Zhi-qiang. Improving the corrosion resistance of MgZn$_{1.2}$Gd$_x$Zr$_{0.18}$ (x=0, 0.8, 1.4, 2.0) alloys via Gd additions [J]. Corrosion Science, 2020, 177: 108962.

[46] KHALFAOUI W, VALERIO E, MASSE J E, AUTRIC M. Excimer laser treatment of ZE41 magnesium alloy for corrosion resistance and microhardness improvement [J]. Optics and Lasers in Engineering, 2010, 48: 926−931.

[47] YANG You-wen, LING Chen-rong, LI Ya-geng, PENG Shu-ping, XIE De-qiao, SHEN Li-da, TIAN Zong-jun, SHUAI Ci-jun. Microstructure development and biodegradation behavior of additively manufactured Mg−Zn−Gd alloy with LPSO structure [J]. Journal of Materials Science & Technology, 2023, 144: 1−14.

[48] DENG Qing-chen, WU Yu-juan, LUO Yuan-hang, SU Ning, XUE Xiao-yu, CHANG Zhi-yu, WU Qian-ye, XUE Yan-ting, PENG Li-ming. Fabrication of high-strength Mg−Gd−Zn−Zr alloy via selective laser melting [J]. Materials Characterization, 2020, 165: 110377.

[49] DAVID S A, BABU S S, VITEK J M. Welding: Solidification and microstructure [J]. JOM, 2003, 55: 14−20.

[50] GRÖBNER J, KOZLOV A, FANG Xi-ya, GENG Jie, NIE Jian-feng, SCHMID-FETZER R. Phase equilibria and transformations in ternary Mg-rich Mg−Y−Zn alloys [J]. Acta Materialia, 2012, 60: 5948−5962.

[51] HUANG Zheng-ren, LIANG Song-mao, CHEN Rong-shi, HAN En-hou. Solidification pathways and constituent phases of Mg−Zn−Y−Zr alloys [J]. Journal of Alloys and Compounds, 2009, 468: 170−178.

[52] BÄR F, BERGER L, JAUER L, KURTULDU G, SCHÄUBLIN R, SCHLEIFENBAUM J H, LÖFFLER J F. Laser additive manufacturing of biodegradable magnesium alloy WE43: A detailed microstructure analysis [J]. Acta Biomaterialia, 2019, 98: 36−49.

[53] YAN Chang-jian, XIN Yun-chang, CHEN Xiao-bo, XU Dao-kui, CHU P K, LIU Chao-qiang, GUAN Bo, HUANG Xiao-xu, LIU Qing. Evading strength−corrosion tradeoff in Mg alloys via dense ultrafine twins [J]. Nature Communications, 2021, 12: 4616.

[54] DING De-yu, DU Yu-hang, TANG Mei-fang, SONG Bo, GUO Ning, ZHANG Hong-ju, GUO Sheng-feng. Corrosion and discharge behavior of Mg−Zn−Mn−Nd alloys as primary Mg−air batteries anode [J]. Transactions of Nonferrous Metals Society of China, 2023, 33: 2014−2029.

[55] XI Guo-qiang, MOU Yu, MA Yan-long, ZHAO Xu-han,

XIONG Ju, MA Kai, WANG Jing-feng. Effect of volume fraction of 18R-LPSO phase on corrosion resistance of Mg−Zn−Y alloys [J]. Transactions of Nonferrous Metals Society of China, 2023, 33: 454−466.

[56] RALSTON K D, BIRBILIS N, DAVIES C H J. Revealing the relationship between grain size and corrosion rate of metals [J]. Scripta Materialia, 2010, 63: 1201−1204.

[57] AHMADKHANIHA D, FEDEL M, HEYDARZADEH SOHI M, DEFLORIAN F. Corrosion behavior of severely plastic deformed magnesium based alloys: A review [J]. Surface Engineering and Applied Electrochemistry, 2017, 53: 439−448.

[58] SONG Dan, MA Ai-bin, JIANG Jing-hua, LIN Ping-hua, YANG Dong-hui, FAN Jun-feng. Corrosion behavior of equal-channel-angular-pressed pure magnesium in NaCl aqueous solution [J]. Corrosion Science, 2010, 52: 481−490.

激光表面熔融处理 Mg−Zn−Y 合金的显微组织与腐蚀行为

彭珍珍[1]，许敏恒[1]，邵晓宏[2]，杨 潇[1]，赵恒虎[1]，梁志敏[1]，汪殿龙[1]，刘 英[1]

1. 河北科技大学 材料科学与工程学院 河北省材料近净成形技术重点实验室，石家庄 050018；
2. 中国科学院 金属研究所 沈阳材料科学国家研究中心，沈阳 110016

摘 要：采用激光表面熔化(LSM)技术提高含粗大、不连续长周期堆垛有序(LPSO)相的 Mg−Zn−Y 合金的耐蚀性能，并对此合金在 LSM 过程中的显微组织演变和凝固行为进行研究。结果表明，LSM 导致原样品中微米级 LPSO 相消失，并使晶粒尺寸从 300 μm 减小到 15 μm，因此，合金的腐蚀速率显著降低。细晶粒由 β 共晶相区、W 相区和层状结构区组成，它们在快速冷却过程中依次形成。枝晶层状结构沿镁基体基面生长，层间由过饱和 α-Mg 相隔开。大型原电池的消失和晶粒细化提高了 Mg−Zn−Y 合金的耐腐蚀性能。

关键词：Mg−Zn−Y 合金；显微组织演变；凝固行为；激光表面熔化；抗腐蚀性能

(Edited by Wei-ping CHEN)